Identifying the optimal spatial distribution of tracers for optical sensing of stream surface flow

Alonso Pizarro[1], Silvano F. Dal Sasso[1], Matthew T. Perks[2], Salvatore Manfreda[3]

[1]Department of European and Mediterranean Cultures, University of Basilicata, Matera, 75100, Italy
5 [2]School of Geography, Politics and Sociology, Newcastle University, Newcastle-upon-Tyne, NE1 7RU, UK
[3]Department of Civil, Architectural and Environmental Engineering, University of Naples Federico II, Naples, 80125, Italy

Correspondence to: Alonso Pizarro (alonso.pizarro@unibas.it)

Abstract. River monitoring is of particular interest as society that faces increasingly complex water management issues.
Emerging technologies have contributed to opening new avenues for improving our monitoring capabilities, but have also
10 generated new challenges for the harmonised use of devices and algorithms. In this context, optical sensing techniques for
stream surface flow velocities are strongly influenced by tracer characteristics such as seeding density and their spatial
distribution. Therefore, a principal research goal is the identification of how these properties affect the accuracy of such
methods. To this aim, numerical simulations were performed to consider different levels of tracer clustering, particle colour
(in terms of greyscale intensity), seeding density, and background noise. Two widely used image-velocimetry algorithms were
15 adopted: i) Particle Tracking Velocimetry (PTV), and ii) Large-Scale Particle Image Velocimetry (LSPIV). A descriptor of
the seeding characteristics (based on seeding density and tracer clustering) was introduced based on a newly developed metric
called the Seeding Distribution Index (SDI). This index can be approximated and used in practice as $SDI = v^{0.1} / \left(\frac{\rho}{\rho_{cv1}} \right)$ where
$v, \rho,$ and ρ_{cv1} are the spatial clustering level, the seeding density, and the reference seeding density at $v = 1$, respectively. A
reduction of image-velocimetry errors was systematically observed for lower values of SDI; and therefore, the optimal frame
20 window (i.e., a subset of the video image sequence) was defined as the one that minimises SDI. In addition to numerical
analyses, a field case study on the Basento river (located in southern Italy) was considered as a proof-of-concept of the proposed
framework. Field results corroborated numerical findings, and error reductions of about 15.9 and 16.1% were calculated -
using PTV and PIV, respectively - by employing the optimal frame window.

1 Introduction

25 Streamflow observations are of enormous importance for environmental protection and engineering practice in general
(Anderson et al., 2006; Manfreda, 2018; Manfreda et al., 2020; Owe, 1985). Such observations are critical for many
hydrological and hydraulic applications. In turn, these data contribute to understanding of more complex processes such as
flash flood dynamics (Perks et al., 2016), the interaction of fish upstream and downstream of dams (Strelnikova et al., 2020),
sediment transport dynamics (Batalla and Vericat, 2009), and bridge scour (Manfreda et al., 2018a; Pizarro et al., 2017a).

Streamflow measurement campaigns are generally expensive and time-consuming, requiring the presence of highly-qualified personnel and forward planning (Tauro et al., 2018). Such approaches are typically based on pointwise measurements performed with flowmeters or acoustic Doppler current profilers (ADCPs) that require the direct placement of the operators or devices into the water. On the one hand, this is necessary to provide a full description of the flow velocity profile, but on the other hand, these field methods might alter the measurements, given the potential interaction of these elements with the flow. Additionally, these standard approaches can be challenging and sometimes impossible to perform at flood conditions when operators and devices are unable to work in-situ due to unfavourable circumstances. This issue has been partially dealt with by the use of non-contact approaches as a modern alternative for river flow monitoring. Progress in the development of non-contact approaches (such as image velocimetry, radars, and microwave systems) has been promising in recent years, opening the possibility for real-time, non-contact flow monitoring. In particular, advancements in image processing techniques have led to improvements of image-based approaches for surface flow velocity (SFV) estimation, and these developments have expanded the range of potential applications. Several techniques, such as Particle Tracking Velocimetry (PTV) and Large-Scale Image Velocimetry (LSPIV), have been proposed and applied in field campaigns to accurately estimate SFV from video acquisitions (Bechle et al., 2012; Huang et al., 2018; Tauro and Salvatori, 2017). In turn, videos can be recorded from different devices (fixed-station located close to the river-section of interest, using cell phones, or onboard Unmanned Aerial Systems (UASs)), allowing an easy and portable way to estimate SFVs and, consequently, river discharge (Kinzel and Legleiter, 2019; Leitão et al., 2018; Manfreda et al., 2018b; Pearce et al., 2020; Perks et al., 2016; Tauro et al., 2015).

The PTV technique revolves around particle identification and tracking (Lloyd et al., 1995) that can be implemented through cross-correlation (Brevis et al., 2011; Lloyd et al., 1995), relaxation (Wu and Pairman, 1995), among other methods. Additionally, particle trajectories can be reconstructed, adding valuable information to the analysis and making it possible to apply trajectory-based filters to ensure realistic trajectories (Eltner et al., 2020; Tauro et al., 2019). On the other hand, LSPIV techniques apply Particle Image Velocimetry (PIV) principles (Adrian, 1991, 2005; Peterson et al., 2008; Raffel et al., 2018) to large scales and natural environments (Fujita et al., 1998). LSPIV recognises and tracks patterns (which can be a group of tracers within a discrete spatial portion of the water surface) instead of single tracers, which are tracked in PTV. As a consequence, PTV adopts an exclusively Lagrangian approach, while PIV employs an Eulerian one.

The use of these techniques is growing in recent years, but it is hard to quantify their accuracy at field scales. This difficulty can be attributed to: i) environmental conditions, which can both deteriorate and enhance the image quality during the acquisition period (Le Coz et al., 2010; Muste et al., 2008); and ii) the characteristics of the tracers/features, such as colour, dimension, shape, seeding density, and their spatial distribution in the field of view (Dal Sasso et al., 2018, 2020; Raffel et al., 2018). PTV and LSPIV need features to identify, match, and track to compute surface flow velocities. High seeding densities are, however, rare in natural environments and, as a consequence, a common practice is the use of artificial tracers to increase the surface seeding in the field of view (Dal Sasso et al., 2018; Tauro et al., 2014, 2017). In this context, Figure 1 shows three different real case-study examples of natural and artificial seedings that tend to cluster. Remarkably, Figure 1.A reports high spatial clustering levels of tracers and complex structures during a flood event at the Tiber river in Italy (Tauro et al., 2017),

whereas Figure 1.B and 1.C present the case when artificial seeding is introduced in the river system for image-velocimetry analysis (Detert et al., 2017; Tauro et al., 2017). More information about the mentioned case studies can be found elsewhere (Perks et al., 2019).
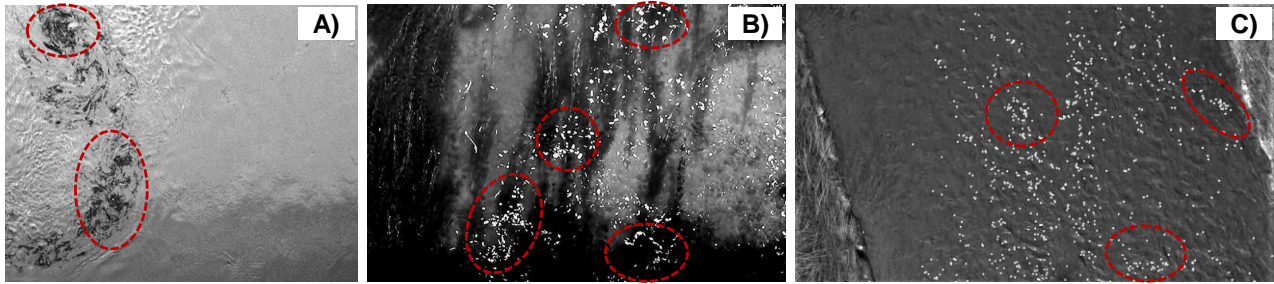
Figure. 1. Examples of moving and clustering structures on the water surface: A) Natural seeding during a flood event at the Tiber river, Italy (Tauro et al., 2017); B) and C) Artificial seeding at low/intermediate flow conditions at Brenta river in Italy (Tauro et al., 2017) and Murg river in Switzerland (Detert et al., 2017), respectively.

The spatial distribution of artificial tracers (hereafter called spatial clustering) is, however, operator-dependent and influenced by their experience, the type of material deployed, and the amount. External environmental and river conditions such as wind and turbulence are also important factors. This issue is extremely relevant for discharge estimates recovered through image-based approaches because velocity errors are transmitted to streamflow estimates. As a consequence, and even when using up-to-date approaches, monitoring complex flows and extreme flood events is still a challenge.

This paper aims to quantify the accuracy of SFV estimates under different seeding densities and spatial clustering levels. To achieve this goal, the following objectives were proposed: i) perform numerical simulations of synthetic tracers to produce 33,600 synthetic images with known seeding characteristics; ii) using these synthetic images, derive a functional relationship between seeding densities, spatial clustering levels, and image velocimetry errors under controlled conditions; iii) analyse footage acquired from the Basento River to determine how variations in seeding characteristics such as seeding density and spatial clustering of tracers influence the image velocimetry errors in a field environment. Finally, iv) apply the function developed in ii) to the Basento River to enable the selection of the optimal image frame sequence to minimise the velocity errors.

The rest of the paper is organised as follows: Section 2 presents the numerical framework for synthetic image generation; a description of the hydrological characteristics of the Basento case study, which is used as a proof-of-concept; and, an outline of the PTV and PIV techniques adopted in the analysis. Section 3 analyses the effects of seeding density and spatial clustering level on image-velocimetry results, using the synthetically generated images, and those of the Basento field case study. Section 4 presents the strengths and limitations of the research and framework adopted in this paper. Conclusions are provided in Section 5.

2 Methods

2.1 Numerical Simulations

Numerical simulations were performed to test two different image-velocimetry algorithms under controlled conditions, minimising the effects of external disturbances. In particular, the influence of tracer/feature properties on the final errors were quantified. Synthetic tracers were randomly distributed in space with a unidirectional and constant velocity. They consist of uniform circular shapes with diameter Dxp ≈ 10 pixels (px) and uniform white colour. Both diameters and colours - in grayscale intensity - were altered with white noise in order to consider more realistic configurations. Their spatial distribution was controlled by a Generalised Poisson Distribution (GPD) with an imposed numerical seeding density λ and spatial clustering level v.

The GPD was first introduced by Efron (1986), allowing the possibility to obtain point events randomly distributed in space with a given variance. The GPD has been used to model randomly distributed events in different studies to describe the spatial characteristics of the landscape and vegetation organisation across climatological gradients (e.g. Good, Rodriguez-Iturbe, and Caylor (2013) and Manfreda, Caylor, and Good (2017)). In this manuscript, the synthetic tracers are assumed to be randomly distributed in space with a mean number λS where S is the considered area. In consequence, the probability mass function that the random number of synthetic tracers, N, will be equal to a number n_i is given by Eq. (1),

$$f_{\text{GPD}(\lambda S)}(n_i) = \frac{1}{C_{\text{GPD}}} \frac{\exp\left(-\frac{\lambda S}{v}\right)}{\sqrt{v}} \left(\frac{\exp(-n_i)\, n_i^{n_i}}{n_i!}\right) \left(\frac{\exp(1)\, \lambda S}{n_i}\right)^{n_i/v}, \tag{1}$$

where λS and v determine the location and the shape of $f_{GPD(\lambda S)}(n_i)$, and C_{GPD} is an integration constant.

Tracers moved with a constant numerically imposed velocity of 15 px/frame along the y-axis and within a grid of 500x500 pixels on a clear water background as representative of real environmental conditions. Tracer diameter was set larger than 2.5 pixels in order to avoid peak locking effects (Cardwell et al., 2011; Dal Sasso et al., 2018; Nobach et al., 2005). Typical tracer dimensions at laboratory and field scales motivated the choice of Dxp ≈ 10 px for image-velocimetry experiments (Tauro et al., 2016).

Synthetic image sequences were generated by varying the number of tracers in the spatial domain, allowing the consideration of 14 different seeding densities ranging from 0.4E-05 particles per pixel (ppp) up to 1.0E-02 ppp. This range of variability was established based on the typical values adopted in field surveys (Tauro and Grimaldi, 2017) and numerical studies (Dal Sasso et al., 2018). Tracer colour (in terms of greyscale intensity) and diameter were altered (by introducing Gaussian white noise with standard deviations equal to 0.05 and 0.3, respectively) to simulate environmental signal noise such as possible changes in luminosity, brightness, and shadows. Figure 2 shows an example of synthetic images generated with different spatial clustering levels and a fixed value of seeding density. In particular, the spatial distribution of tracers moves from an over-dispersed organisation ($v = 0.5$), through a Poisson random distribution ($v = 1$) and an under-dispersed one ($v = 100$) to a super under-dispersed distribution ($v = 200$). Figure 2 (A, B, C and D) presents the original synthetic generation on the

120   clear water background, while Figure 2 (E, F, G and H) shows the pre-processed images, enhancing the contrast between tracers and background (See Section 2.3). Furthermore, each numerical experiment involved generating 20 images, and each configuration was run 10 times. The spatial clustering level ranges from 0.5 to 200 (12 different values), and in consequence, 33,600 synthetic images were generated (14 different λ, 12 different υ, 20 images per configuration, and 10 times each configuration).

125
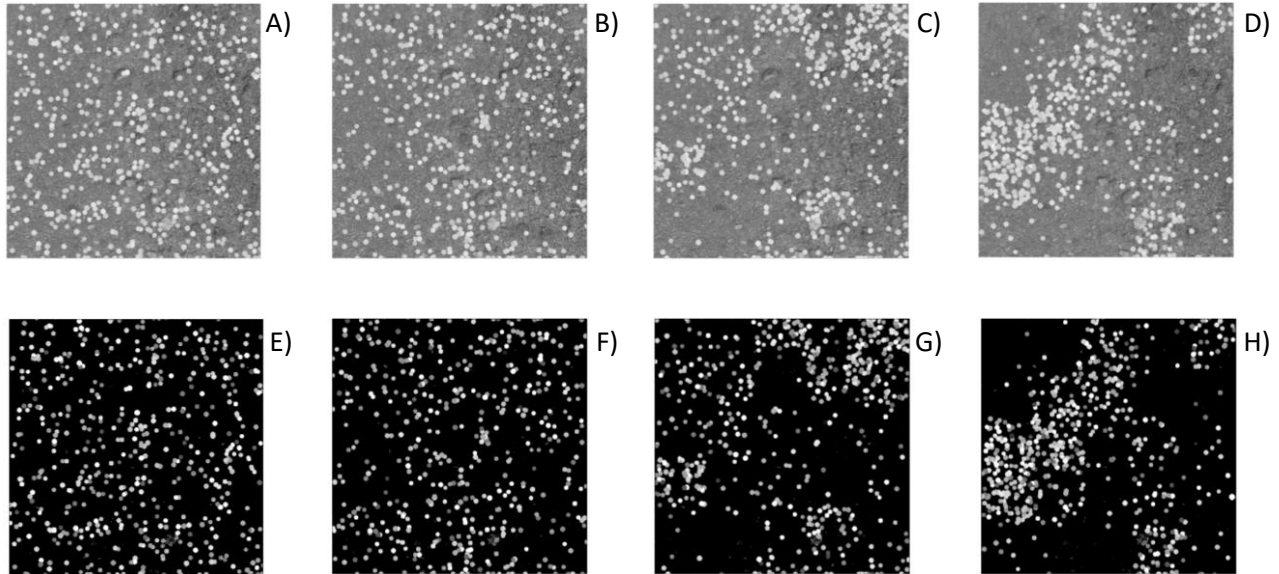
Figure. 2. Synthetic generations of spatial distribution of tracers assuming different values of the parameter υ = 0.5 (over-dispersed distribution - Fig 2.A, E), 1.0 (Poisson random distribution - Fig 2.B, F), 100 (under-dispersed distribution - Fig 2.C, G), and 200 (super under-dispersed distribution - Fig 2.D, H). Fixed value of the seeding density λ = 2.02E-03. The generation was carried out adopting a background in the images to provide more realistic conditions (A, B, C, D). Thereafter, images have been pre-processed
130   **to increase the contrast and better visualise tracers (E, F, G, H).**

2.2 Proof-of-concept: The Basento case study

A field survey on the Basento River (Basilicata region, southern Italy) was carried out to test the outcomes of numerical simulations under natural conditions. The cross-section considered for the measurements is located in the upper portion of the basin (catchment area of about 127 km^2) (Figure 3). The main river flow characteristics, at the time of video acquisition, were:
135   i) river discharge: 0.61 m^3/s; ii) maximum flow depth: 0.38 m; iii) river width: 6.0 m; iv) maximum surface flow velocity: 0.68 m/s; and, v) average surface flow velocity: 0.40 m/s. Data were acquired using a DJI Phantom 3 Professional Quadcopter (DJI, Shenzhen, China) equipped with an integrated 4k UHD (ultra-high-definition) video recording camera and a 3-axis stabilised system. Video acquisition was performed using a Sony EXMOR 1/2.3" CMOS sensor and a greyscale video was captured from the UAS platform with a resolution of 1920x1080 px (i.e., full high definition - FHD). The frame rate was set to 24
140   frames per second (fps). Reference objects, useful for image scale calibration and stabilisation, were positioned at visible locations on the riverbanks. The calibration factor converting pixels to meters was estimated, taking into consideration those objects with known-a-priori dimensions. The ground sampling distance (GSD) was, therefore, computed as 0.005 m/px.

Benchmark velocity measurements were performed using a current meter (SEBA F1, SEBA Hydrometrie GmbH & Co, Kaufbeuren, Germany), in the proximity of the water surface, at 11 different locations across the river cross-section. The accuracy of measurements was within 2% of the measured values, corresponding to 0.001 and 0.013 m/s for the minimum and maximum velocities in question. The spanning distance between the respective measurements was 0.5 m. Each measurement was made over a fixed acquisition period of 30 seconds. River discharge was estimated according to ISO 748 (1997), using the velocity-area method. The cross-section was divided into panels of equal width and, for each panel, the velocity was measured at 20%, 60% and 80% of the panel depth. Artificial seeding was deployed onto the water surface, giving the possibility to create complex floating structures. Two operators were involved in the process, and artificial tracers made of wood chips were used to enhance particle seeding the region of interest (ROI).

The videos captured with the UAS were first stabilised using an automatic feature selection method that identifies features in frame pairs, matching them to compute possible values of translation and rotation. The Features from Accelerated Segment Test (FAST) detection algorithm was applied to identify features on an ad-hoc ROI. To improve the feature matching accuracy at each step, the method utilises the Random Sample Consensus (RANSAC) filter to remove unacceptable correspondences. The application of the stabilisation algorithm allowed the effects of camera movements to be reduced throughout the duration of the video. Planar errors considering differences in translation and rotation were computed taking the first frame as the reference target. On average, the reduction due to the stabilisation process goes from 64 to 7 px for the Basento case study. Therefore, movement in the original video is reduced by around 89%. The stabilisation algorithm does not require Ground Control Points (GCPs) to be applied. Rather, it performs the detection of features automatically, making the stabilisation process a good alternative for non-experienced users.

The Basento River presented low-flow conditions leading us to subsample the original video from 24 to 12 fps. The choice of the appropriate frame rate was made to ensure, on the one hand, a frame-by-frame displacement bigger than particle dimension and, on the other hand, to minimise the effects of camera movement between frame pairs on the calculation of surface velocity. The footage was acquired in greyscale and a pre-processing procedure was applied using contrast stretching techniques to enhance the visibility of the artificial tracers against the background. For this purpose, GIMP (the GNU Image Manipulation Program) was utilised to adjust brightness and contrast. This procedure eliminated a large amount of noise caused by external reflections, improving the number of tracers identified and thus cross-correlation in the ROI. Figure 3.B shows a composite example of the original frame in grayscale, overlain by a pre-processed image covering the extent of the active channel (darker area overlapping the original frame).
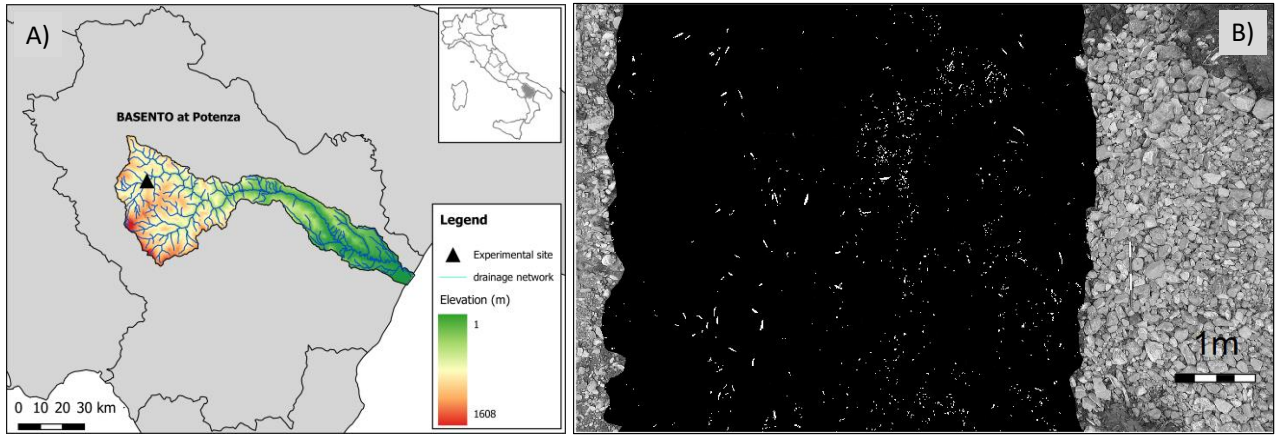
Figure. 3. A) Basento river and its drainage basin with an indication of the measurement location (Basento at Potenza). B) Grayscale footage acquired with a DJI Phantom 3 Pro (river banks) and corresponding footage after the pre-processing (river flow) aimed at enhancing contrast for particle identification.

2.3 Image velocimetry analysis

PTV analyses were carried out employing a command-line version of PTVLab software (Brevis et al., 2011) that was automated in order to handle the number of synthetic images. Tracer detection was performed using the particle Gaussian mask correlation method (Ohmi and Li, 2000). Parameters for particle diameter and reflectance intensity were set equal to 8 px and 70, respectively. Particle tracking was implemented using a cross-correlation algorithm (Wu and Pairman, 1995). The interrogation area (IA) was set at 20 px, cross-correlation threshold at 0.7, and neighbour similarity percentage at 25%. PTV parameter settings were slightly modified under field conditions due to the differences between the numerical and field datasets. In particular, the average tracer dimension in the field conditions was estimated as 5 px and therefore, the particle diameter was set equal to 4 px and the IA at 25 px.

PIV analyses were performed employing a command-line version of PIVLab software (Thielicke and Stamhuis, 2014). The PIV algorithm was applied, for both numerical and field analysis, using the Fast Fourier Transform (FFT) with a three-pass standard correlation method (search and interrogation areas of 128x64, 64x32 and 32x16 px and with 50% overlap). Additionally, the 2x3-point Gaussian fit was employed to estimate the sub-pixel displacement peak. These parameters were carefully chosen to ensure correct identification and tracking of synthetic tracers.

Finally, the quality of the results was determined by examining the magnitude of the errors that were computed as:

$$\epsilon = 100 \times \frac{(u_c - u_R)}{u_R}, \tag{2}$$

where u_C is the computed velocity and u_R is the numerically imposed (numerical case taken as reference) or measured (field case) velocity.

3 Results and Discussion

3.1 Numerical Analysis

The performance of PTV and PIV tracking algorithms was assessed by the calculation of errors (considering the imposed numerical surface velocity) to test how the seeding density and spatial distribution of tracers influenced the final velocity estimates. No post-processing method was applied to filter the spatiotemporal velocity results. The ROI was taken as the original dimension of the synthetic image generation, i.e. 500x500 px. The processing times, considering all the synthetically generated images, for PTV and PIV analyses were 18,548 and 4,736 seconds, respectively. The same hardware (Processor i7-8700 CPU @ 3.20 GHz 3.19 GHz and RAM 32 GB) was used for both image-velocimetry analyses, leading to a fair comparison between them. PTV computing time was almost four times higher than PIV under the circumstances considered in this study. For all cases, PTV and PIV techniques systematically underestimated the imposed numerical velocity independently of the seeding density and spatial clustering level under consideration. Consequently, only negative errors were observed with numerical results, in agreement with previously published work (Dal Sasso et al., 2018). This can be due to the use of a static background that may introduce sporadic zero velocity vectors. Figure 4 shows the PTV and PIV error results with different values of seeding densities and spatial clustering levels. A comparison between PTV and PIV is shown in Figure 4.A, where each data point is associated with a colour that is scaled based on the numerically imposed seeding density adopted in the generation of synthetic images. A strong dependence between image-velocimetry results and seeding density was observed: errors can be reduced by increasing the seeding density. In all cases, PTV outperformed PIV under the synthetic conditions analysed in this study. These findings also support those of Tauro, Piscopia, and Grimaldi (2017) who found that PTV outperformed PIV in two different field case studies (Brenta and Tiber Rivers). It is however noteworthy that the results we present here refer to a single synthetic experiment that, although realistic, is not representative of any field condition. Therefore, further investigation with a larger set of idealised and field circumstances should be carried out to generalise the obtained results.
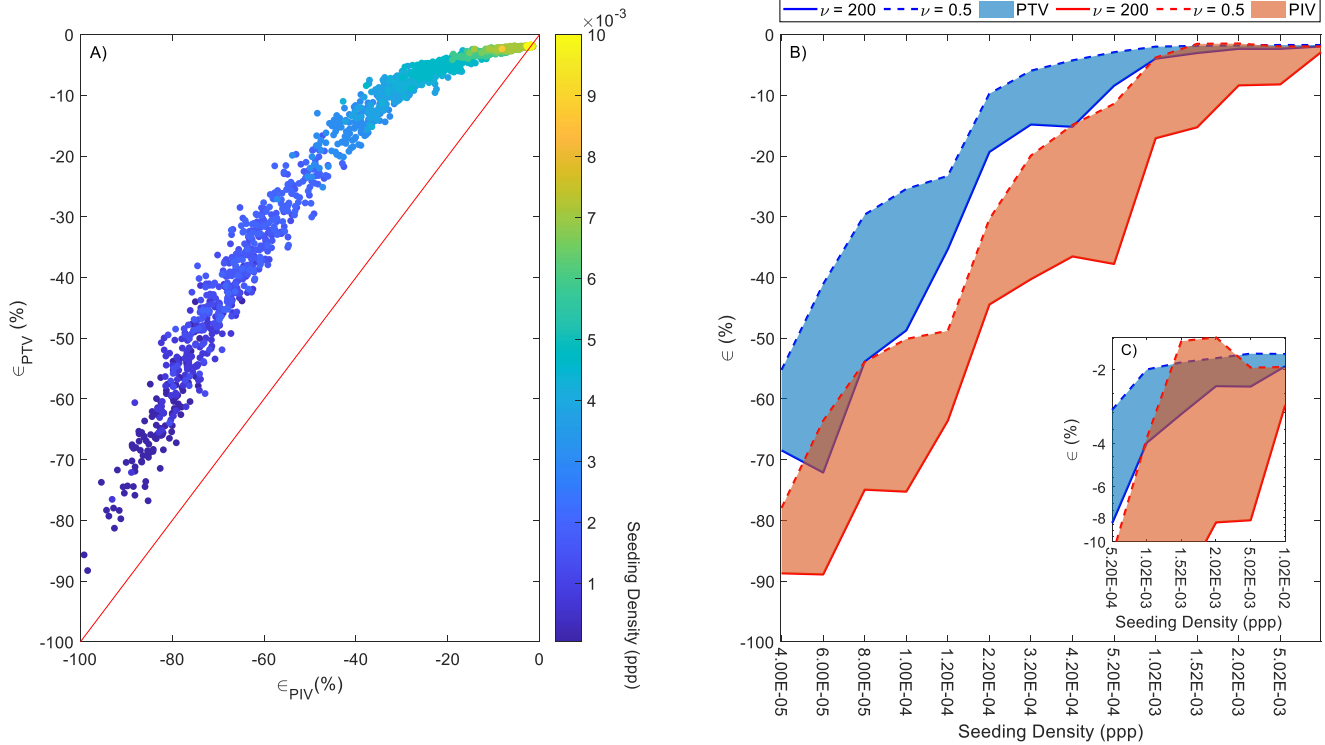
215

Figure 4. Comparison of PTV and PIV results using synthetic images with different values of seeding density and spatial clustering level. Only negative errors were observed with numerical results. A) PTV vs PIV errors (ϵ_{PTV} and ϵ_{PIV}, respectively). Each data point is associated with a colour that is scaled based on the numerically imposed seeding density adopted in the numerical generation of synthetic images. B) Envelope error curves and areas in function of seeding density and level of spatial clustering ν. The blue and
220 **orange colours are associated with PTV and PIV results, respectively. Dashed and solid lines are associated with $\nu = 0.5$ and $\nu = 200$, respectively. C) Zoom of the right upper portion of B).**

Figure 4.B shows the envelope error curves (and areas between them) for a range of seeding densities and level of spatial clustering ν. The blue and orange colours are associated with PTV and PIV error results, while dashed and solid lines are associated with $\nu = 0.5$ and $\nu = 200$, respectively. For the sake of simplicity, Figure 4.B only shows the extreme cases when ν
225 $= 0.5$ and $\nu = 200$; nevertheless, all the other cases (with ν values between these two extremes) were confined within these envelope curves. Error results of both techniques were influenced by ν, with a higher spatial clustering level tending to deteriorate the accuracy of image-velocimetry results, producing higher errors and associated variability across the range of seeding densities. When the sensitivity of PIV and PTV to changes in ν are compared, PIV is generally more sensitive than PTV, as demonstrated by the greater distance between $\nu = 0.5$ and $\nu = 200$ lines for a given seeding density, and by the orange
230 shaded area being greater than the blue. The minimum seeding density leading to the lowest errors (around $2 - 3\%$) depended on ν. These errors were taken as reference values after which an asymptotic behaviour was observed. As a consequence, this minimum seeding density concept was termed reference seeding density in the rest of the paper. For instance, considering the

PIV case, the reference seeding density values were 1.52E-03 and 1.02E-02 for $\nu = 0.5$ and $\nu = 200$, respectively. The reference seeding density values for PTV were 1.02E-03 and 2.02E-03 for $\nu = 0.5$ and $\nu = 200$, respectively.

235   These numerical results are useful to visualise more-in-depth trends under controlled flow conditions, avoiding external disturbances. Results demonstrated that the minimum required seeding density to produce an error equal or lower than 3% differs slightly between the two techniques. We used this percentage as a reference error in order to derive a reference seeding density associated with a known error. It was observed that PIV required 1.52E-03 ppp, while PTV needed about 1.02E-03 ppp to reach the same error. Notably, seeding densities lower than 1.0E-03 produced larger errors (larger than 3%) and

240   consequently, flows should be seeded at least this density in field campaigns for optimal implementation of the methods. This practice should be adopted if at all possible since typical natural flows are not characterised by abundant transiting features, with maybe the exception of high flows. Furthermore, the effective seeding density (defined as the seeding that the algorithms are genuinely able to identify, match, and track) is always lower than the one transiting onto the water surface and therefore, extra seeding is recommended practice. However, we are aware that this recommendation might not be practical in all

245   conditions since fixed cameras can operate remotely without the necessity to be in-person at the field site, and deploying material in wide channels or difficult-to-access areas might be challenging.

Following dimensional considerations, a model of the image-based errors can be formulated. Since the only variables considered in this study were the spatial clustering level and the seeding density, it is hypothesised that these errors depend on only these variables. In functional form

$$f(\epsilon, \nu, \rho, \rho_{cv1}) = 0, \tag{3}$$

250   where f is a generic function, and ρ and ρ_{cv1} are the seeding density and the reference seeding density at $\nu = 1$ (Poisson case taken as a reference). According to the Buckingham-π theorem, Eq. (3) can be rewritten in terms of dimensionless parameters as follows:

$$\epsilon = f\left(\nu, \frac{\rho}{\rho_{cv1}}\right). \tag{4}$$

The function f is usually considered as a multiplication of power laws (Buckingham, 1914; Evans, 1972; Melville and Sutherland, 1988; Pizarro et al., 2017b). In this study, we partially follow this approach and also hypothesise that the functional

255   relationship f is described by a two-parameter exponential function:

$$\epsilon = c_1(1 - e^{-c_2 SDI}), \tag{5}$$

$$SDI = \nu^{k_1}\left(\frac{\rho}{\rho_{cv1}}\right)^{k_2},$$

where SDI is the multiplication of power laws; and, c_1, c_2, k_1, k_2 are fitting coefficients. Model performance was quantified by means of the root mean square error (RMSE) and the Nash-Sutcliffe efficiency (NSE) for prediction of the image-velocimetry errors. In turn, the fitting coefficients were calibrated using the MATLAB genetic algorithm optimising RMSE.

260 Table 1 summarises the results of the calibration process for both PTV and PIV, while Figure 5 shows the image-velocimetry errors as a function of SDI, and observed versus computed errors. Figure 5 indicates that SDI can correctly reproduce the main dynamics of the image-velocimetry errors, reporting low RMSE values in calibration (5.34 and 5.77% for PIV and PTV, respectively). A visual inspection of Figure 5.A1 and 5.B1 shows that increasing SDI values leads to higher errors for both image-velocimetry techniques. Figure 5.A2 and 5.B2 also show that the predictive capacity of Eq. (5) is higher at low PTV

265 and PIV error values.

Even though PIV and PTV work differently, the fitted values in Eq. (5) were similar. Remarkably, k_1 and k_2 showed that the dimensionless SDI parameter can be approximated and used in practice as

$$\text{SDI} = v^{0.1} / \left(\frac{\rho}{\rho_{\text{cv1}}} \right).$$

(7)

Furthermore, considering that the errors are minimised when SDI takes low values, SDI can be used in field conditions as a descriptor to choose the optimal portion of a video to analyse in order to minimise the errors in image-velocimetry estimates

270 as a function of seeding density and spatial clustering level. This novel idea is explored in the next subsection, taking the Basento River as a proof-of-concept case study.

Table 1. Calibrated values of c_1, c_2, k_1, k_2 and model performances in terms of RMSE (%) and NSE. PTV and PIV calibration results. ρ_{cv1} values for PIV and PTV were taken from Figure 4 and are 1.52E-03 and 1.02E-03, respectively.

	c_1	c_2	k_1	k_2	RMSE (%)	NSE
PTV	-71.87	0.04	0.10	-1.09	5.77	0.92
PIV	-78.49	0.07	0.10	-1.06	5.34	0.97

275
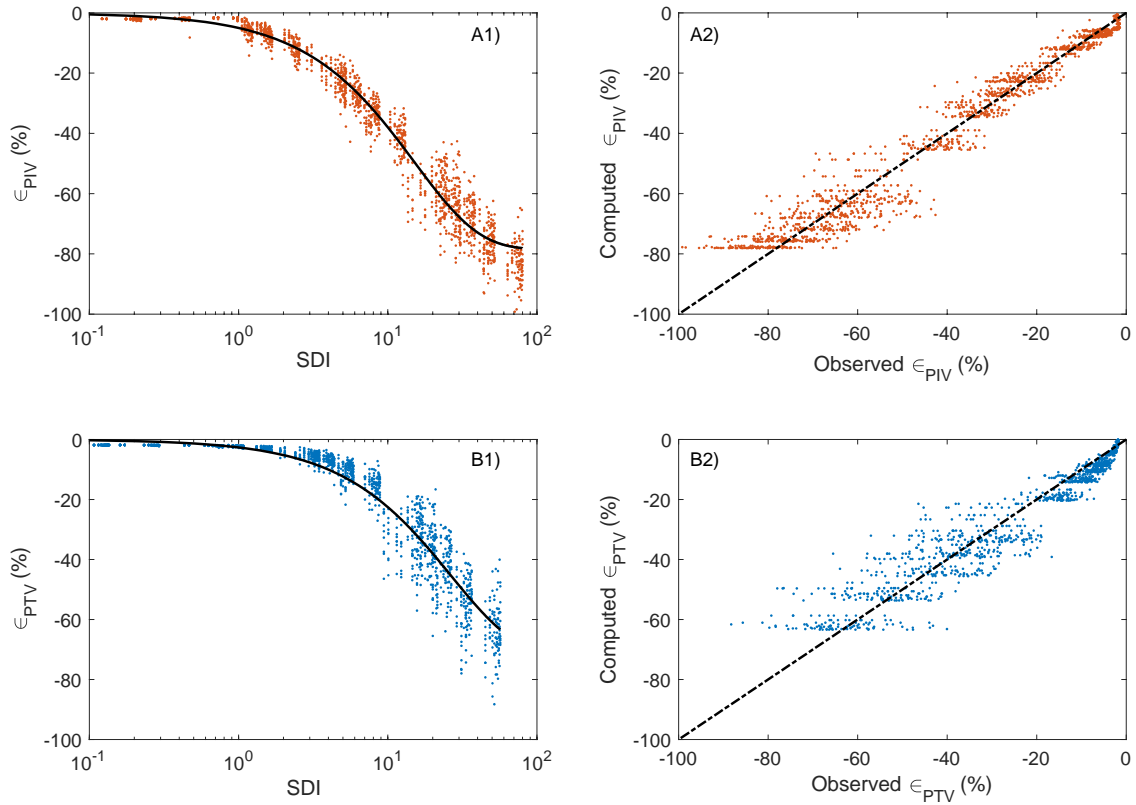
Figure 5. Image-velocimetry errors as a function of SDI (A1 and B1) and observed versus computed errors (A2 and B2). Blue and orange colours are related to PTV and PIV numerical error results. Solid lines represent Eq. (5), while the dashed lines are the perfect agreement between observed and computed image-velocimetry errors.

3.2 Field Campaign: The Basento case study

Outcomes of the numerical analysis were tested on a real case study in order to identify the best temporal window (i.e., a subset of the video sequence) for image velocimetry analyses. The case study was selected due to the spatial distribution of tracers varying significantly during the recording period, making it subjective to manually select the optimal frames for analysis. Figure 6 displays a pre-processed frame with the location of the measuring points using standard field equipment (from L1 to L11). These surface flow velocity measurements were taken as reference velocities for PTV and PIV benchmarking. Figure 6.B and 6.C show a zoom of the ROI and the identification of transiting features, respectively. An example of identified features is presented in Figure 6.D. In this figure, the number of features, their relative positions and associated areas were identified using an ad-hoc algorithm developed by Dal Sasso et al. (2020). Moving features – that can be blobs, regions of uniform intensity, or local corners – are detected and processed to derive seeding properties (i.e., empirical seeding densities and spatial distribution of tracers) on a frame-by-frame basis even if shapes and dimensions of the tracers vary considerably. Using this approach, the empirical spatial clustering level (i.e., the empirical equivalent to that used in the numerical simulations), was quantified through the spatial dispersion index $D^*(= D/D_{Poisson} = [\text{Var}(N)/E(N)]/1$, where $\text{Var}(N)$ and

E(N) are the variance and mean values of the number of tracers N, respectively, computed in sub-patches of the same size). This metric is normally measured to quantify whether a set of events are clustered or dispersed. Important to notice, D^* is assumed as an estimator of ν due to their similar properties such as $D^* = \nu = 1$ which means features follow a Poisson distribution, while $D^* < 1$ ($\nu < 1$) and $D^* > 1$ ($\nu > 1$) follow an over- and under-dispersed spatial distribution, respectively.
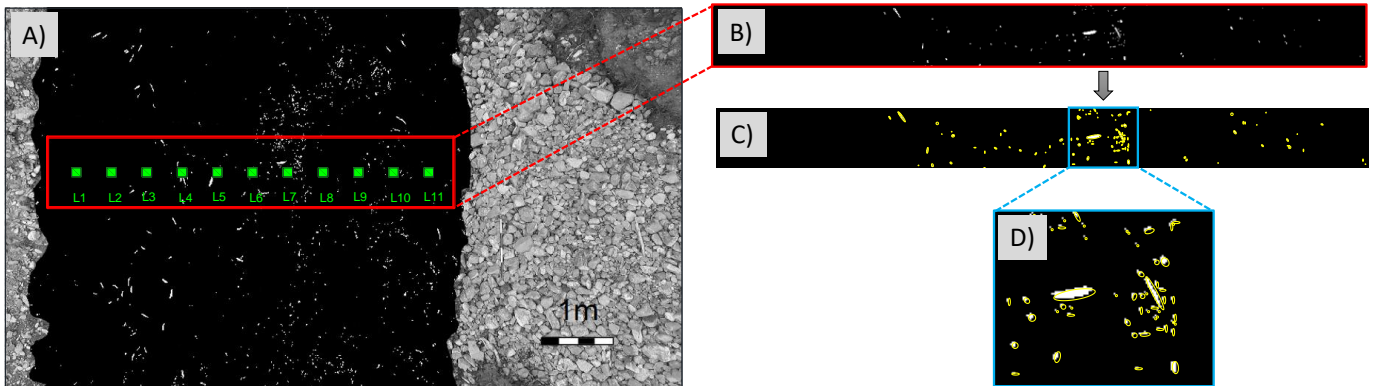
Figure 6. A) Pre-processed frame indicating the ROI and the reference measuring locations for benchmark purposes. The isolation of the ROI is presented in B), while in C) an example of identified features on the water surface. D) Zoom of an arbitrary portion of the ROI with the identified features.

Figure 7 shows a comprehensive overview of the seeding behaviour during the 200 frames considered for the analysis. Figure 7.A and 7.B present the seeding density in ppp, and the dispersion index D^* computed as a function of the frame number. The minimum and maximum values for seeding density were 1.3E-04 and 2.9E-03 ppp, while those for the dispersion index were 4.1 and 57.3. Additionally, the estimated mean area of features (computed frame-by-frame and inside the ROI) varied between 1.5 and 3.5 cm^2 approximately.
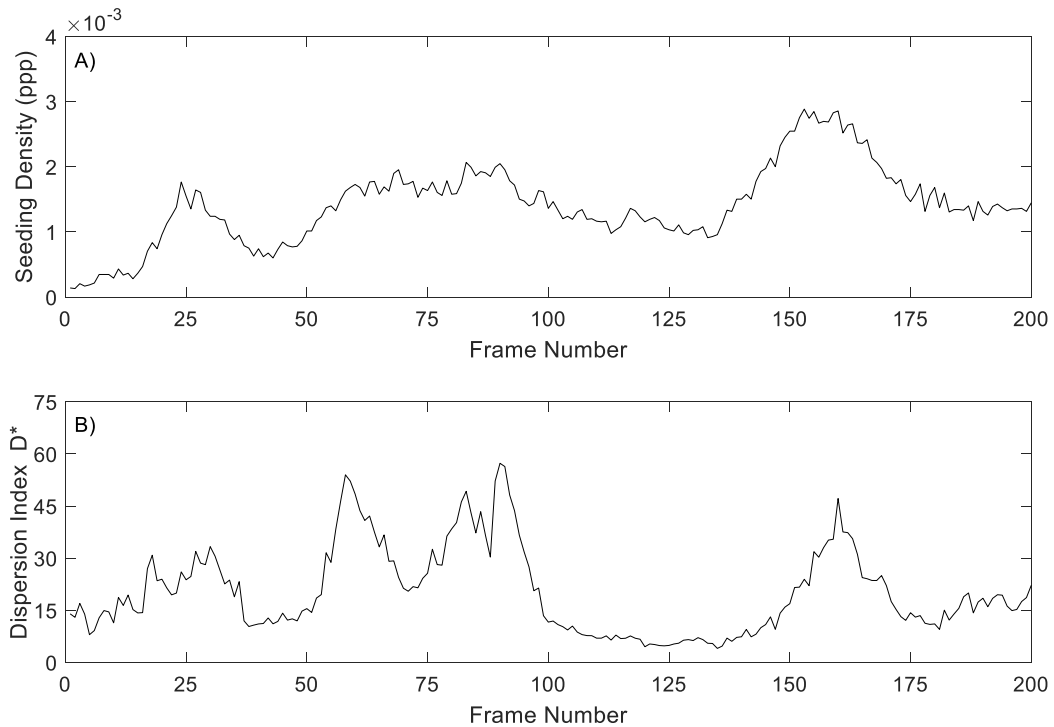
Figure 7. Overview of seeding characteristics on the ROI of the Basento River during the acquisition time: A) Seeding density in ppp, B) Dimensionless dispersion index D*.

The approach mentioned above made it possible to compute SDI and correctly identify the worst and best part of the video for

310   image velocimetry analysis. A moving frame window length of 100 frames was arbitrarily chosen, on which an average dispersion index D* and seeding density were computed. This decision was motivated to increase the odds of populating the entire ROI with features. The empirical SDI was then calculated as $\mathrm{SDI} = \overline{D}^{0.1}/\left(\frac{\bar{\rho}}{\rho_{\mathrm{cv1}}}\right)$, where $\overline{D}$ and $\bar{\rho}$ are the average-in-100-frames dispersion index and seeding density, respectively. Figure 8.A depicts SDI in function of the frame windows. Triangle markers correspond with the minimum and maximum value of SDI and their respective locations (82-181 and 1-100,

315   respectively). Figure 8.A shows the particular case of PTV; nevertheless, PIV presented similar results. The locations of the minimum and maximum SDI values was, therefore, unaffected by the image-velocimetry technique under consideration.
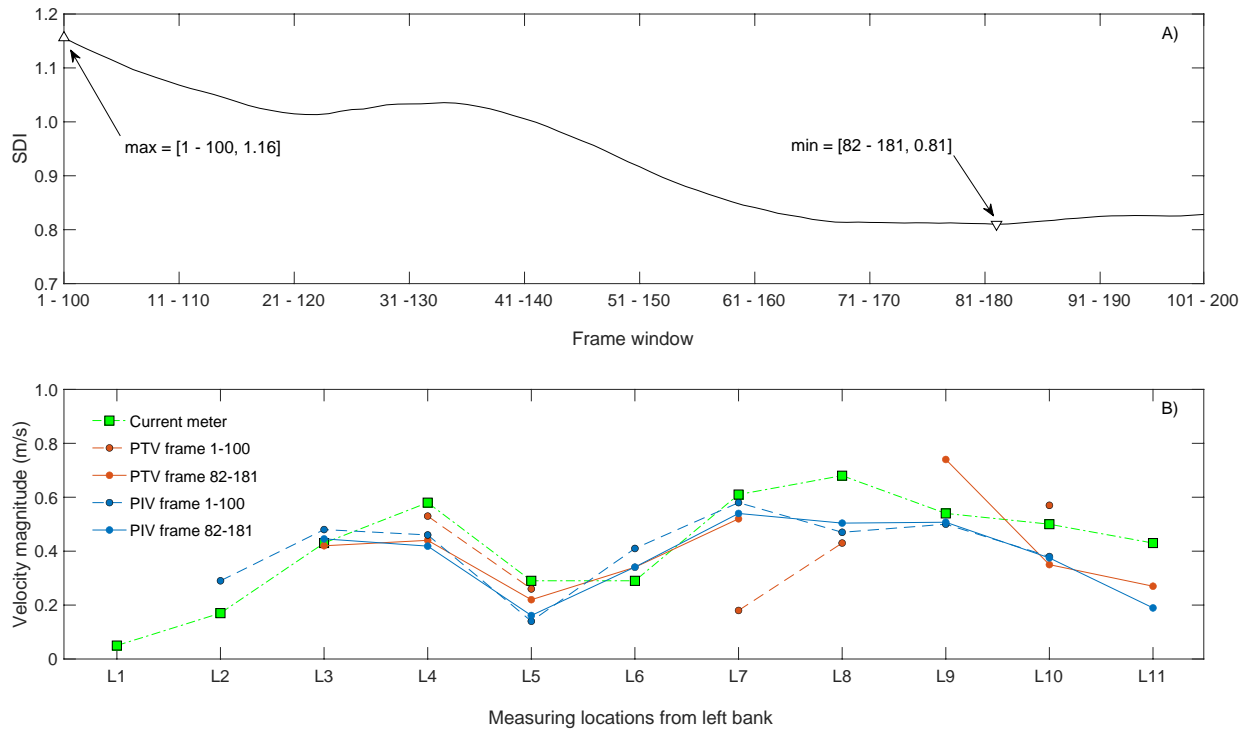
Figure 8. A) SDI as a function of the frame window considering 100 frames. Triangle markers correspond with the minimum and maximum value of SDI. Their locations were 82-181 and 1-100, respectively. Particular case of PTV, whereas PIV showed similar
320 **results and the locations of the minimum and maximum SDI values were unaffected by the image-velocimetry technique. B) Comparison between PTV and PIV data for experiments on the Basento River. Values recorded with the current meter are also reported for a rapid visual assessment (green squares). Blue and orange colours represent PTV and PIV data.**

Image-based velocity results were averaged in a block of 30x30 cm^2 for a fair comparison among PTV, PIV, and benchmark velocity values. The measuring locations corresponded with the centre of the blocks. Computed velocities across the cross-
325 section and reference velocities are reported in Figure 8.B. The blue and orange colours are associated with PTV and PIV results, respectively (same colours used within numerical results for consistency and fast visual comparison). Green squares are the velocities measured using the current meter. Notably, the measuring location L1 had no computed velocity values due to the lack of features transiting on this part of the ROI, whereas only PIV was able to compute velocities at L2. This issue can be explained due to the inherent property of PIV to identify and track non-seeded features such as ripples and other structures
330 transiting on the water surface. Interestingly, and in agreement with numerical results, 80% (frames 1-100) and 75% (frames 82-182) of the computed velocity measuring locations underestimated the reference velocities using PTV. Similarly, results using PIV were 67 and 78%, respectively. Therefore, a close agreement was observed with the numerical results that systematically presented underestimations of computed velocities in comparison with the numerically imposed one. The computed errors using PTV, PIV, and the total number of frames available were 23.93% and 23.69%, respectively. Moreover,
335 adopting the optimal frame window ensured that image-velocimetry measurements were produced for a greater or equal

proportion of the channel than that produced by using frames 1 - 100 (PTV: 72.7% vs 45.5% of the channel width; PIV: 81.8% vs 81.8%).

Both image-velocimetry approaches correctly captured the mean behaviour of velocities across the cross-section. Table 2 presents summarised information of the average-in-100-frames seeding density and dispersion index as well as the initial and final frame used for image-velocimetry purposes. The SDI value is also presented as well as the absolute average error across the cross-section. As expected from numerical analyses, an error reduction respect to the worst scenario of about 15.9% (PTV) and 16.1% (PIV) was found on the Basento case study by employing the optimal frame window that minimises SDI. It is therefore recommended that SDI is used as a descriptor of the optimal portion of a video to analyse.

Table 2. Overview of features characteristics, minimum and maximum SDI values, and absolute errors using PTV and PIV. Values in parenthesis correspond with the error reduction respect to the worst scenario using the optimal frame window.

Frames (from – to)	$\overline{\rho}$ (ppp)	$\overline{D}$	SDI PTV	SDI PIV	Absolute average Error (%) PTV	Absolute average Error (%) PIV	Absolute Error Eq. (5) (%) PTV	Absolute Error Eq. (5) (%) PIV
1 - 100	1.2E-03	26.1	1.16	1.72	27.72	28.74	3.70	8.91
82 - 181	1.7E-03	18.2	0.81	1.21	23.31 (15.9)	24.11 (16.1)	2.61 (29.5)	6.36 (28.6)

Finally, considering numerical findings, field image-based estimates presented larger errors in comparison with numerical results for the respective same values of SDI (last two columns of Table 2). This is despite the average seeding density being relatively high (~1.5E-03) and the average dispersion index relatively low (~20). Possible reasons for deteriorations in PTV and PIV estimates can be attributed to other variables such as video stabilisation issues, noise due to different environmental conditions (e.g., intermittent and different levels of illumination, water reflections, and presence of shadows), and different shapes and dimensions of features (stressing the matching and tracking process between consecutive frames). In this regard, Dal Sasso et al. (2020) recently introduced metrics for the quantification of seeding characteristics needed to enhance image-velocimetry performances in rivers. Among them, the seeding density, spatial clustering level, and coefficient of variation of tracers' dimension were statistically significantpredictors of velocity estimation accuracy. These issues should be the subject of further investigation, along with the application of these ideas to case studies with very different field conditions to assess the uncertainty of computed surface velocities and remote river flow estimates.

4 Strengths and limitations

One of the main strengths of this study is the introduction of the new dimensionless SDI index, which combines seeding characteristics – seeding density and spatial clustering of tracers – for image-velocimetry purposes. A numerical framework of synthetically generated images was adopted to isolate seeding effects on the performance of PIV and PTV analysis. This numerical framework allowed the generation of moving tracers with the possibility to vary the seeding density and spatial clustering of tracers. Additionally, one field case study was used to test and validate numerical findings. However, among

365   other limitations, the numerical framework considered a constant and unidirectional imposed velocity only. Besides, PIV and PTV were set to run using a single configuration (e.g., PIV used FFT with a three-pass correlation method with fixed SA and IA rather than other combinations of SA and IA or an ensemble correlation method). The field case study was artificially seeded to enhance the identification and tracking of moving patterns on the water surface. Interestingly, the dispersion index D^* was used as an empirical estimator of the numerical clustering level of tracers ν. D^* and ν share some interesting properties,

370   which are useful to characterise under- and over-dispersed spatial distribution of tracers in practical applications. Finally, the errors computed using all frames available (frames 1 - 200) versus the optimal frame window (frames 82 - 181) were of the same order of magnitude, even though the number of frames used with SDI was the half of the total available. As a consequence, the quality of the seeding characteristics seemed to be more critical than the duration of the footage. Of course, many other factors might affect the quality of the videos and consequently, the performance of image velocimetry estimates,

375   but this assessment focuses specifically on the spatial distribution of tracers. In the field, other factors such as illumination conditions, shading on the scene, light reflections, presence of turbulent fluxes, vibration of the camera – among others – could further affect overall quality of the analysis, and these should be the subject of further assessment.

5 Conclusions

In this paper, we investigated the performances of PTV and PIV for surface flow velocity estimation. Synthetic generation of

380   33,600 images was performed to test image-velocimetry techniques under different levels of seeding density and tracer spatial clustering. In all numerical cases, velocity results systematically underestimated the imposed numerical velocity. A general trend was observed in which increasing the seeding density and decreasing the level of spatial clustering improved results. The main advantage of the numerical approach adopted is the controlled conditions in which the analyses can be conducted, minimising the effects of external disturbances. Based on numerical findings, seeding densities lower than 1.0E-03 produced

385   larger errors and consequently, flows should be extra-seeded in field campaigns for optimal implementation of image velocimetry methods. Additionally, the dimensionless SDI index was introduced as a descriptor of the optimal portion of the video to analyse using the studied image-based techniques. Based on numerical results, SDI can be approximated and used in practice as $SDI = \nu^{0.1} / \left(\frac{\rho}{\rho_{cv1}} \right)$, where $\nu, \rho,$ and ρ_{cv1} are the spatial clustering level, the seeding density, and the converging seeding density at $\nu = 1$, respectively. A reduction of image-based errors was observed with lower values of SDI.

390   The Basento field case study (located in southern Italy) was considered as a proof-of-concept of the proposed framework. Seeding characteristics were empirically estimated using a novel algorithm recently developed by the authors, opening the possibilities of more refined analyses. The number of features, relative positions, and associated areas were saved for the computation of the empirical seeding densities and spatial clustering levels. The empirical SDI values were then computed, and two extreme cases were considered for velocimetry comparison purposes: i) the one considering the maximum value of

395   SDI (worst case), and ii) the one related to the minimum SDI (best case). Field results corroborated numerical findings, and

an error reduction of about 15.9 and 16.1% was achieved for PTV and PIV approaches respectively by using the optimal frame window that minimises SDI for the Basento case study.

Interestingly, field image-based estimates presented larger errors than numerical results for the respective same values of SDI. Possible reasons for deteriorating PTV and PIV estimates can be attributed to other variables such as: i) video stabilisation

400   issues; ii) variable levels of illumination, water reflections, and presence of shadows; and, iii) different shapes and dimensions of seeding features, stressing the importance of the feature matching and tracking process between consecutive frames. Further assessment is required to evaluate the significance of these factors in contributing to the uncertainty in image-velocimetry estimates across a range of hydrological and environmental conditions.

Code availability: The code used to compute the SDI index as well as seeding metrics is available at Pizarro et al. (2020b),
405   https://doi.org/10.17605/OSF.IO/8EGQW.

Data availability: Numerical and field data used in this study are available at Pizarro et al. (2020a), http://doi.org/10.5281/zenodo.3761859.

Author contributions: AP conceptualised the study, wrote the scripts, processed and analysed the data, and drafted the paper. SD analysed the field data. SM coordinated the research activities and defined the research project. SD, MP, and SM
410   contributed to the writing and reviewed the manuscript.

Competing interests: The authors declare no conflict of interest.

Acknowledgements: This work was funded by the COST Action CA16219 "HARMONIOUS—Harmonization of UAS techniques for agricultural and natural ecosystems monitoring".

References

415   Adrian, R.: Particle-Imaging Techniques For Experimental Fluid-Mechanics, Annu. Rev. Fluid Mech., doi:10.1146/annurev.fluid.23.1.261, 1991.

Adrian, R. J.: Twenty years of particle image velocimetry, Exp. Fluids, 39(2), 159–169, 2005.

Anderson, K. E., Paul, A. J., McCauley, E., Jackson, L. J., Post, J. R. and Nisbet, R. M.: Instream flow needs in streams and rivers: The importance of understanding ecological dynamics, Front. Ecol. Environ., doi:10.1890/1540-
420   9295(2006)4[309:IFNISA]2.0.CO;2, 2006.

Batalla, R. J. and Vericat, D.: Hydrological and sediment transport dynamics of flushing flows: Implications for management in large Mediterranean rivers, River Res. Appl., doi:10.1002/rra.1160, 2009.

Bechle, A., Wu Chin, H., Liu, W.-C. and Kimura, N.: Development and Application of an Automated River-Estuary Discharge

Imaging System, J. Hydraul. Eng., 138(4), 327–339, doi:10.1061/(ASCE)HY.1943-7900.0000521, 2012.

425   Brevis, W., Niño, Y. and Jirka, G. H.: Integrating cross-correlation and relaxation algorithms for particle tracking velocimetry, Exp. Fluids, 50(1), 135–147, 2011.

Buckingham, E.: On physically similar systems; Illustrations of the use of dimensional equations, Phys. Rev., doi:10.1103/PhysRev.4.345, 1914.

Cardwell, N. D., Vlachos, P. P. and Thole, K. A.: A multi-parametric particle-pairing algorithm for particle tracking in single
430   and multiphase flows, Meas. Sci. Technol., 22(10), 105406, 2011.

Le Coz, J., Hauet, A., Pierrefeu, G., Dramais, G. and Camenen, B.: Performance of image-based velocimetry (LSPIV) applied to flash-flood discharge measurements in Mediterranean rivers, J. Hydrol., 394(1), 42–52, 2010.

Dal Sasso, S. F., Pizarro, A., Samela, C., Mita, L. and Manfreda, S.: Exploring the optimal experimental setup for surface flow velocity measurements using PTV, Environ. Monit. Assess., 190(8), doi:10.1007/s10661-018-6848-3, 2018.

435   Dal Sasso, S. F., Pizarro, A. and Manfreda, S.: Metrics for the quantification of seeding characteristics to enhance image velocimetry performance in rivers, Remote Sens., doi:10.3390/rs12111789, 2020.

Detert, M., Johnson, E. D. and Weitbrecht, V.: Proof-of-concept for low-cost and non-contact synoptic airborne river flow measurements, Int. J. Remote Sens., doi:10.1080/01431161.2017.1294782, 2017.

Efron, B.: Double exponential families and their use in generalized linear regression, J. Am. Stat. Assoc.,
440   doi:10.1080/01621459.1986.10478327, 1986.

Eltner, A., Sardemann, H. and Grundmann, J.: Technical Note: Flow velocity and discharge measurement in rivers using terrestrial and unmanned-aerial-vehicle imagery, Hydrol. Earth Syst. Sci., 24(3), 1429–1445, doi:10.5194/hess-24-1429-2020, 2020.

Evans, J. H.: Dimensional Analysis and the Buckingham Pi Theorem, Am. J. Phys., doi:10.1119/1.1987069, 1972.

445   Fujita, I., Muste, M. and Kruger, A.: Large-scale particle image velocimetry for flow analysis in hydraulic engineering applications, J. Hydraul. Res., 36(3), 397–414, 1998.

Good, S. P., Rodriguez-Iturbe, I. and Caylor, K. K.: Analytical expressions of variability in ecosystem structure and function obtained from threedimensional stochastic vegetation modelling, Proc. R. Soc. A Math. Phys. Eng. Sci., doi:10.1098/rspa.2013.0003, 2013.

450   Huang, W. C., Young, C. C. and Liu, W. C.: Application of an automated discharge imaging system and LSPIV during typhoon events in Taiwan, Water (Switzerland), doi:10.3390/w10030280, 2018.

ISO, I. S. O.: 748, Measurement of Liquid Flow in Open Channel—Velocity-Area Methods. 1997, 1997.

Kinzel, P. J. and Legleiter, C. J.: sUAS-based remote sensing of river discharge using thermal particle image velocimetry and bathymetric lidar, Remote Sens., doi:10.3390/rs11192317, 2019.

455   Leitão, J. P., Peña-Haro, S., Lüthi, B., Scheidegger, A. and Moy de Vitry, M.: Urban overland runoff velocity measurement with consumer-grade surveillance cameras and surface structure image velocimetry, J. Hydrol., doi:10.1016/j.jhydrol.2018.09.001, 2018.

Lloyd, P. M., Stansby, P. K. and Ball, D. J.: Unsteady surface-velocity field measurement using particle tracking velocimetry, J. Hydraul. Res., 33(4), 519–534, 1995.

460 Manfreda, S.: On the derivation of flow rating curves in data-scarce environments, J. Hydrol., doi:10.1016/j.jhydrol.2018.04.058, 2018.

Manfreda, S., Caylor, K. K. and Good, S. P.: An ecohydrological framework to explain shifts in vegetation organization across climatological gradients, Ecohydrology, doi:10.1002/eco.1809, 2017.

Manfreda, S., Link, O. and Pizarro, A.: A theoretically derived probability distribution of scour, Water (Switzerland), 465 doi:10.3390/w10111520, 2018a.

Manfreda, S., McCabe, M. F., Miller, P. E., Lucas, R., Madrigal, V. P., Mallinis, G., Dor, E. Ben, Helman, D., Estes, L., Ciraolo, G., Müllerová, J., Tauro, F., de Lima, M. I., de Lima, J. L. M. P., Maltese, A., Frances, F., Caylor, K., Kohv, M., Perks, M., Ruiz-Pérez, G., Su, Z., Vico, G. and Toth, B.: On the use of unmanned aerial systems for environmental monitoring, Remote Sens., doi:10.3390/rs10040641, 2018b.

470 Manfreda, S., Pizarro, A., Moramarco, T., Cimorelli, L., Pianese, D. and Barbetta, S.: Potential advantages of flow-area rating curves compared to classic stage-discharge-relations, J. Hydrol., 124752, 2020.

Melville, B. W. and Sutherland, A. J.: Design method for local scour at bridge piers, J. Hydraul. Eng., 114(10), 1210–1226, 1988.

Muste, M., Fujita, I. and Hauet, A.: Large-scale particle image velocimetry for measurements in riverine environments, Water 475 Resour. Res., 44(4), 2008.

Nobach, H., Damaschke, N. and Tropea, C.: High-precision sub-pixel interpolation in particle image velocimetry image processing, Exp. Fluids, 39(2), 299–304, 2005.

Ohmi, K. and Li, H.-Y.: Particle-tracking velocimetry with new algorithms, Meas. Sci. Technol., 11(6), 603, 2000.

Owe, M.: Long-term streamflow observations in relation to basin development, J. Hydrol., 78(3–4), 243–260, 1985.

480 Pearce, S., Ljubičić, R., Peña-Haro, S., Perks, M., Tauro, F., Pizarro, A., Dal Sasso, S., Strelnikova, D., Grimaldi, S., Maddock, I., Paulus, G., Plavšić, J., Prodanović, D. and Manfreda, S.: An Evaluation of Image Velocimetry Techniques under Low Flow Conditions and High Seeding Densities Using Unmanned Aerial Systems, Remote Sens., doi:10.3390/rs12020232, 2020.

Perks, M., Sasso, S. F. D., Hauet, A., Coz, J. Le, Pearce, S., Peña-Haro, S., Tauro, F., Grimaldi, S., Hortobágyi, B., Jodeau, M., Maddock, I., Pénard, L. and Manfreda, S.: Towards harmonization of image velocimetry techniques for river surface 485 velocity observations, Earth Syst. Sci. Data Discuss., doi:10.5194/essd-2019-133, 2019.

Perks, M. T., Russell, A. J. and Large, A. R. G.: Technical note: Advances in flash flood monitoring using unmanned aerial vehicles (UAVs), Hydrol. Earth Syst. Sci., doi:10.5194/hess-20-4005-2016, 2016.

Peterson, S. D., Chuang, H. S. and Wereley, S. T.: Three-dimensional particle tracking using micro-particle image velocimetry hardware, Meas. Sci. Technol., doi:10.1088/0957-0233/19/11/115406, 2008.

490 Pizarro, A., Samela, C., Fiorentino, M., Link, O. and Manfreda, S.: BRISENT: An Entropy-Based Model for Bridge-Pier Scour Estimation under Complex Hydraulic Scenarios, Water, doi:10.3390/w9110889, 2017a.

Pizarro, A., Ettmer, B., Manfreda, S., Rojas, A. and Link, O.: Dimensionless effective flow work for estimation of pier scour caused by flood waves, J. Hydraul. Eng., 143(7), doi:10.1061/(ASCE)HY.1943-7900.0001295, 2017b.

Pizarro, A., Dal Sasso, S. F., Perks, M. T. and Manfreda, S.: Data on spatial distribution of tracers for optical sensing of stream surface flow (Version 0.1), [Dataset] Zenodo, doi:10.5281/zenodo.3761859, 2020a.

Pizarro, A., Dal Sasso, S. F., Perks, M. T. and Manfreda, S.: Identifying the optimal spatial distribution of tracers for optical sensing of stream surface flow (Version 0.1), [codes] OSF, doi:10.17605/OSF.IO/8EGQW, 2020b.

Raffel, M., Willert, C. E., Scarano, F., Kähler, C. J., Wereley, S. T. and Kompenhans, J.: Particle image velocimetry: a practical guide, Springer., 2018.

Strelnikova, D., Paulus, G., Käfer, S., Anders, K.-H., Mayr, P., Mader, H., Scherling, U. and Schneeberger, R.: Drone-Based Optical Measurements of Heterogeneous Surface Velocity Fields around Fish Passages at Hydropower Dams, Remote Sens., doi:10.3390/rs12030384, 2020.

Tauro, F. and Grimaldi, S.: Ice dices for monitoring stream surface velocity, J. Hydro-environment Res., 14, 143–149, 2017.

Tauro, F. and Salvatori, S.: Surface flows from images: ten days of observations from the Tiber River gauge-cam station, Hydrol. Res., 48(3), 646–655, 2017.

Tauro, F., Porfiri, M. and Grimaldi, S.: Orienting the camera and firing lasers to enhance large scale particle image velocimetry for streamflow monitoring, Water Resour. Res., 50(9), 7470–7483, 2014.

Tauro, F., Pagano, C., Phamduy, P., Grimaldi, S. and Porfiri, M.: Large-scale particle image velocimetry from an unmanned aerial vehicle, IEEE/ASME Trans. Mechatronics, 20(6), 3269–3275, 2015.

Tauro, F., Petroselli, A., Porfiri, M., Giandomenico, L., Bernardi, G., Mele, F., Spina, D. and Grimaldi, S.: A novel permanent gauge-cam station for surface-flow observations on the Tiber River, Geosci. Instrumentation, Methods Data Syst., 5(1), 241–251, 2016.

Tauro, F., Piscopia, R. and Grimaldi, S.: Streamflow Observations From Cameras: Large-Scale Particle Image Velocimetry or Particle Tracking Velocimetry?, Water Resour. Res., 53(12), 10374–10394, 2017.

Tauro, F., Selker, J., Van De Giesen, N., Abrate, T., Uijlenhoet, R., Porfiri, M., Manfreda, S., Caylor, K., Moramarco, T., Benveniste, J., Ciraolo, G., Estes, L., Domeneghetti, A., Perks, M. T., Corbari, C., Rabiei, E., Ravazzani, G., Bogena, H., Harfouche, A., Broccai, L., Maltese, A., Wickert, A., Tarpanelli, A., Good, S., Lopez Alcala, J. M., Petroselli, A., Cudennec, C., Blume, T., Hut, R. and Grimaldia, S.: Measurements and observations in the XXI century (MOXXI): Innovation and multi-disciplinarity to sense the hydrological cycle, Hydrol. Sci. J., doi:10.1080/02626667.2017.1420191, 2018.

Tauro, F., Piscopia, R. and Grimaldi, S.: PTV-Stream: A simplified particle tracking velocimetry framework for stream surface flow monitoring, Catena, doi:10.1016/j.catena.2018.09.009, 2019.

Thielicke, W. and Stamhuis, E. J.: PIVlab – Towards User-friendly, Affordable and Accurate Digital Particle Image Velocimetry in MATLAB, J. Open Res. Softw., doi:10.5334/jors.bl, 2014.

Wu, Q. X. and Pairman, D.: A relaxation labeling technique for computing sea surface velocities from sea surface temperature, IEEE Trans. Geosci. Remote Sens., 33(1), 216–220, 1995.